PAPER

Check for updates

Natural product-integrated microneedle patch for rheumatoid arthritis treatment through anti-inflammation and angiogenesis suppression†

Peng Hua,[a] Suleixin Yang,[a] Lin Yu, [ID][b] Yongzhuo Huang [ID][c] and Meiwan Chen [ID] *[a]

Synovitis and angiogenesis are two essential pathological factors that synergistically aggravate rheumatoid arthritis (RA), in which the highly inflammatory environment promotes new blood vessel formation while constant angiogenesis renders recruitment of more inflammatory macrophages. Herein, we developed a micelle-embedded dissolvable microneedle to realize both anti-inflammation and anti-angiogenesis effects for enhanced anti-arthritis therapy. Anti-arthritis natural products, berberine (Ber) and sinomenine (Sin), were encapsulated in the reactive oxygen species (ROS)-responsive micelles (B/S-TMs) and self-assembled using thioketal-modified amphiphilic copolymer PLGA-TK-PEG, followed by their integration into a carboxymethyl cellulose-based microneedle to achieve effective transdermal delivery and rapid cargo release. B/S-TMs were accumulated in the RA joint *via* passive targeting, and they released Ber and Sin through thioketal bond cleavage under a high ROS level environment. Interestingly, Ber or Sin individually exerted anti-inflammatory effect *via* simultaneously promoting M2 macrophage polarization and anti-angiogenesis effect by decreasing the endothelial cell migration and tube formation. The combined Ber and Sin further amplified these effects. The therapeutic microneedle patch (B/S-TM@MN) significantly decreased the expression of CD68-positive macrophages and CD31-stained blood vessel, attaining improved anti-arthritis efficacy compared with monotherapies in the collagen-induced arthritis (CIA) mouse model. Our work represents a promising strategy for targeting multiple pathological factors for enhanced anti-RA therapy.

1. Introduction

Rheumatoid arthritis (RA) is a chronic autoimmune disorder distinguished by persistent joint inflammation, progressive cartilage degradation and consequential bone erosion.[1,2] Inflammation and angiogenesis are two essential pathological changes observed in RA, which constantly promote the development and progression of this devastating disease.[3,4] Notably, inflammation and angiogenesis are two closely related processes that possess a positive feedback loop.[5,6] In particular, activated macrophages and invasive fibroblast-like synoviocytes produce proinflammatory mediators to shape the

highly inflammatory environment, which enhance the vascular permeability and lead to new blood vessel formation to facilitate the delivery of oxygen, nutrients, and inflammatory cells to the synovial pannus.[7,8] Moreover, gradually occurring angiogenesis leads to recruitment of more inflammatory macrophages and secreted inflammatory factors in the inflamed synovium, which will aggravate RA.[3,9] Current therapies that exclusively target inflammation suppress pannus growth inadequately owing to unaddressed angiogenesis, leading to unsatisfactory therapeutic outcome. Therefore, the simultaneous inhibition of both inflammation and angiogenesis, targeting multiple pathological features, may represent a potential strategy for effective RA treatment.

Berberine (Ber) and sinomenine (Sin) are bioactive alkaloids that are isolated from *Coptis chinensis* and *Sinomenium acutum*, respectively, and they have been broadly applied in RA treatment owing to their low cost, multiple target capability and low side effects.[10–13] Recent studies have reported multiple pharmacological effects of Ber and Sin, including anti-inflammation, anti-angiogenesis and immunomodulatory effects.[14–17] Compared with the anti-inflammatory roles of Ber and Sin for RA treatment, their anti-angiogenesis effects have

[a]State Key Laboratory of Quality Research in Chinese Medicine, Institute of Chinese Medical Sciences, University of Macau, Macau SAR, China.
*E-mail: mwchen@um.edu.mo*
[b]State Key Laboratory of Molecular Engineering of Polymers, Department of Macromolecular Science, Fudan University, Shanghai 200438, China
[c]Zhongshan Institute for Drug Discovery, Shanghai Institute of Materia Medica, Chinese Academy of Sciences, Zhongshan 528437, China
†Electronic supplementary information (ESI) available. See DOI: https://doi.org/10.1039/d5bm00036j
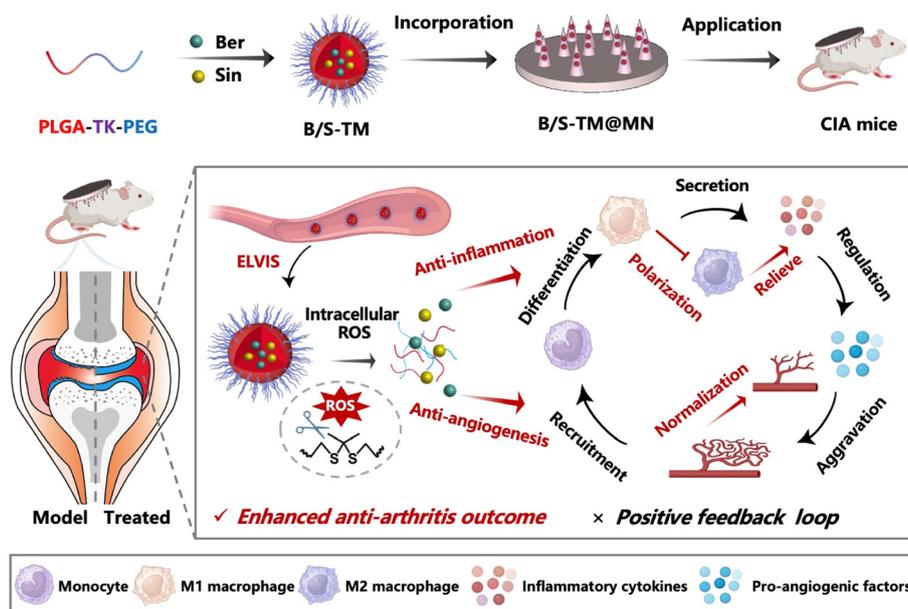
Scheme 1 Schematic of the fabrication procedures of B/S-TM@MN, and the therapeutic mechanism of B/S-TM@MN *via* simultaneous inflammation and angiogenesis inhibition for enhanced anti-arthritis outcome.

been rarely investigated for alleviating RA symptoms. Notably, the mono anti-angiogenesis treatment is confronted with various challenges owing to the ignorance of etiological factors and the drug resistance of single antiangiogenic agents in angiogenic diseases.[18–20] Thus, it is necessary to investigate multiple RA-related pharmacological activities of Ber and Sin, and accordingly, the possibility of dual drug combination to deal with the complexity of RA treatment.

As an emerging transdermal delivery method, Microneedle (MN) has shown promising applications in autoimmune diseases, including systemic sclerosis,[21] systemic lupus erythematosus[22] and rheumatoid arthritis[23,24] owing to the advantages of self-administration, reduced pain and side effects, and versatile therapeutic options. Among the various types of MN, dissolvable MN (DMN) manufactured with natural polymers, such as carboxymethyl cellulose, hyaluronic acid, and chondroitin sulfate, have exhibited a high drug loading efficiency, excellent biocompatibility, and ease of loading various drugs and micro/nanoparticles.[25–27] Considering the poor water solubility, non-synchronous pharmacokinetic behavior, and low bioavailability of free Ber and Sin, endogenous-stimuli-responsive micelles for RA treatment is a promising carrier to co-encapsulate Ber and Sin due to their merits, including their improved solubility, increased RA joint accumulation based on extravasation through leaky vasculature and subsequent inflammatory cell-mediated sequestration (ELVIS) effect, and attaining controllable drug release at target sites.[28–30] Hence, the micelle-incorporated microneedle patch provides a more effective and safer approach to improve the combined RA treatment.

In this study, a carboxymethyl cellulose-fabricated dissolvable microneedle (denoted as B/S-TM@MN) was developed for inhibiting inflammation and angiogenesis. The amphiphilic block copolymer PLGA-TK-PEG was self-assembled into reactive oxygen species (ROS)-responsive micelles to co-encapsulate Ber and Sin, which was then incorporated into MN. The loaded B/S-TM was rapidly released due to the dissolvability of carboxymethyl cellulose after skin insertion of MN, and was then absorbed by blood vessels in the corium layer. B/S-TM can effectively accumulate in the inflamed joints owing to the ELVIS effect, and release dual drugs in response to the high ROS level in the microenvironment of RA joints, relying on the cleavage of thioketal groups to avoid the off-target systematic toxicity. The combination of Ber and Sin effectively alleviated inflammation, as revealed by macrophage repolarization from M1 to M2 and reduction in pro-inflammatory cytokines. It also inhibited angiogenesis as indicated by the decreased endothelial cell migration and tube formation. Furthermore, the *in vivo* anti-inflammation and anti-angiogenesis effect of B/S-TM was also validated. Overall, B/S-TM@MN achieved obvious anti-arthritis efficacy *in vitro* and *in vivo*, providing novel insights on efficient RA treatment (Scheme 1).

2. Materials and methods

2.1. Materials

Berberine, sinomenine and sodium carboxymethyl cellulose (M.W. 90 000) were obtained from Aladdin (Shanghai, China). $PLGA_{10k}$-TK-PEG_{2k} was procured from Xi'an Ruixi Biological Technology Co., Ltd (Xi'an, China). Coumarin 6 and DiR were purchased from Macklin Co., Ltd (Shanghai, China). Kolliphor® P 188, lipopolysaccharide (LPS), and vascular endothelial growth factor (VEGF) were acquired from Sigma-Aldrich Co., Ltd (St Louis, MO, USA). FITC-labeled anti-mouse CD86

and APC-labeled anti-mouse CD206 were obtained from BioLegend Inc. (San Diego, CA, USA). RAW264.7 and HUVEC cells were obtained from American Type Culture Collection (ATCC, Rockville, USA), while FLS was purchased from Jenniobio Biotechnology (Guangzhou, China).

2.2. Preparation of B/S-TM

B/S-TM was synthesized through the solvent emulsification evaporation method.[31] Briefly, 1 mg Ber and 1 mg Sin were dissolved in 400 μL methanol and stirred for 10 min, which were added to 2 mL dichloromethane containing $PLGA_{10k}$-TK-PEG_{2k} (20 mg mL^{-1}). The homogeneous mixture was transferred to 1.5% poloxamer 188 solution. The combined solution was homogenized by ultrasound for a duration of 3 minutes, following specific parameters: interval time of 5 seconds, ultrasound time of 5 seconds, power set at 40%, and temperature maintained at 4 °C. Subsequently, the mixture was vacuum dried at room temperature, and the residue was rehydrated with 1 mL of deionized water for 30 minutes to achieve a micellar solution. As controls, blank TM, B-TM, S-TM and C6-labeled TM were also prepared using the same procedure without adding drugs or by adding Ber, Sin and C6, respectively.

2.3. Characterization of B/S-TM

The particle size and ζ-potential of B/S-TM were assessed using a Malvern Zetasizer (Nano ZS90, Malvern, UK), and the morphology was observed by transmission electron microscope (TEM, Ht-7800, Hitachi, Tokyo, Japan). The stability of B/S-TM was evaluated by monitoring the change in the size for 7 days. The drug release behaviors of Ber and Sin from B/S-TM were monitored through HPLC (Waters e2695, Milford MA, USA), both in the presence and the absence of H_2O_2. For berberine, we employed a mobile phase of 0.2% orthophosphoric acid and acetonitrile at a ratio of 36 : 64 (v/v) with a detection wavelength of 360 nm. In addition, the mobile phase consisting of 0.1% phosphoric acid and acetonitrile (45 : 55, v/v) at the detection wavelength of 261 nm were employed to detect sinomenine.

2.4. Preparation and characterization of B/S-TM@MN

The B/S-TM@MNs were fabricated through a micro-molding process, as per previously established protocols.[32] Initially, 300 μL of sodium carboxymethylcellulose solution (10%, w/v) containing B/S-TM was carefully poured into the MN mold, and centrifuged at a speed of 3000 rpm for 30 min at 4 °C. The excess solution was scraped away. The process was repeated by pouring, centrifuging, and removing extra solution three times. Finally, the blank carboxymethylcellulose solution was poured as the supporting layer. The B/S-TM@MN was obtained after drying for a whole day before demolding. B/S-TM@MN was examined using a fluorescent microscope (Olympus, Japan), and was observed by scanning electron microscope (SEM, Zeiss Sigma, Germany). The mechanical strength of blank MN, B-TM@MN, S-TM@MN and B/S-TM@MN was determined through a texture analyzer (TMS-PRO, FTC, VA, USA) to record the breaking forces of each needle.

2.5. *In vitro* cytotoxicity evaluation

The cytotoxicity of free Ber, Sin, B-TM and S-TM was evaluated against RAW 264.7, HUVEC cells and FLS. Briefly, RAW 264.7, HUVEC cells and FLS were seeded in a 96-well plate and incubated overnight, and were then treated with Ber, Sin, B-TM, and S-TM at various concentrations in the range of 0–100 μg mL^{-1} for 24 h. The relative cellular viability was determined by conducting standard MTT assays.

2.6. Cellular uptake of C6-labeled TM in RAW 264.7 and HUVEC cells

In vitro cellular internalization of C6-labeled TM was studied by fluorescence imaging and flow cytometry. Briefly, RAW 264.7 or HUVEC cells were seeded in the 24-well plate for incubation overnight. Subsequently, RAW 264.7 cells were induced into M1 phenotype through the stimulation of 1 μg mL^{-1} LPS for 24 h. Then, M0 and M1 phenotype macrophages, as well as HUVEC cells, were treated with free C6 and C6-labeled TM for 0.5, 1, 2, 4 h, respectively. The cells were rinsed with PBS and further stained by Hoechst 33342. After staining and washing, the internalization of C6-labeled TM was observed through DMI8 inverted fluorescent microscope (Leica, Germany) and the quantitative analysis was performed by flow cytometry (Cytoflex, Beckman, USA).

2.7. Anti-inflammatory characterization of B/S-TM

The stimulated RAW 264.7 cells by LPS were incubated with PBS, B-TM, S-TM or B/S-TM at an equal concentration of Ber/Sin (5 μg mL^{-1}) for a day. The cells were collected and treated with CD16/32 to block Fc-receptors, and were subsequently incubated with anti-CD86 antibody (FITC-label) and anti-CD206 antibody (APC-label) for 30 min. The CD86 and CD206 expression levels were measured by FCS. The cell culture supernatants were collected to analyze the levels of proinflammatory cytokines, such as TNF-α, IL-6, and IL-1β by ELISA kits (Jiancheng Bioengineering Institute, Nanjing, China).

2.8. Tube formation assay

The anti-angiogenesis effect of B/S-TM was investigated through tube formation assay, according to the reported literature.[19] Corning® Matrigel® basement membrane matrix (Corning #356234) was dissolved at 4 °C beforehand. Then, Matrigel was gently added to the 96-well plate and incubated at 37 °C for 30 min. HUVECs were seeded and treated with PBS, B-TM, S-TM and B/S-TM at a Ber/Sin concentration of 5 μg mL^{-1}. 20 ng mL^{-1} of VEGF was supplemented to support tube formation. The tube formation images were captured after 12 h by a DMI8 inverted microscope (Leica, Wetzlar, Germany). The quantitative analysis of the branch point and total capillary length related to tube formation were analyzed by ImageJ software with angiogenesis analysis plugin.

2.9. Migration assay

HUVECs or FLS were seeded and cultured overnight. FLS were pre-treated with TNF-α (10 ng mL^{-1}) to be activated into the

aggressive phenotype.[23] Subsequently, HUVECs or FLS were treated with PBS, B-TM, S-TM or B/S-TM at a Ber/Sin concentration of 5 μg mL^{-1} for 24 h. The collected cells were suspended in DMEM without the addition of FBS, and the cell suspension was introduced into the upper chamber of Transwell inserts with a polycarbonate membrane (6.5 mm diameter, 8 μm pore, Corning #3422) at a density of 5×10^4 cells per insert. Each insert was then placed in a 24-well plate comprising 750 μL of DMEM supplemented with 20% FBS in the lower chamber. Following an incubation period of 24 h, cells in the upper chamber were carefully removed using a cotton swab. The cells migrated to the lower side of the Transwell insert were fixed in 4% paraformaldehyde for 15 min, and stained by 0.1% crystal violet for 30 min. After PBS washing, images were captured with the microscope (Olympus). The numbers of migrated HUVECs were determined by counting cells in three distinct representative fields for each insert with the aid of ImageJ software.

2.10. Scratch assay

HUVECs and FLS were distributed within 12-well plates at a density of 1×10^5 per well, and were cultivated until confluent. The scratch wound in each well was created by a p200 pipet tip. After being gently washed with PBS, HUVECs were cultured by DMEM containing 10% FBS and treated with PBS, B-TM, S-TM or B/S-TM at a Ber/Sin concentration of 5 μg mL^{-1}. The migration areas at the beginning and at 24 h were captured by DMI8 inverted microscope, and the wound closure ratios were quantified by ImageJ software.

2.11. Collagen-induced arthritis mouse

Male Balb/c mice aged 6 to 7 weeks were sourced from Guangdong Experimental Animal Center (Guangzhou, China). The animals were kept under standard laboratory conditions, following a 12-hour light and 12-hour dark cycle, and were provided with unrestricted access to food and water. All animal experiments were approved by the Experimental Animal Ethics Committee of the Zhuhai campus of Zunyi Medical University (Permit Number: ZHSC-2-2023-044), and were performed in accordance with the National Research Council's Guide for the Care and Use of Laboratory Animals.

In order to induce the collagen-induced arthritis (CIA) mice model, a solution of type II collagen (2 mg mL^{-1}, Chondrex) and complete Freund's adjuvant (CFA, 4 mg mL^{-1}, Chondrex) were emulsified at a concentration ratio of 1 : 1. The emulsified solution was then injected intradermally at the base of each mouse's tail. After 7 days, a booster injection was administered intradermally using an emulsion of type II collagen and incomplete Freund's adjuvant (IFA, Chondrex). To monitor RA progression, the clinical score of RA was assessed every three days until the endpoint of the animal study. The process of assessing the clinical score was conducted in a blinded manner, adhering strictly to established scoring criteria.[33]

2.12. Distribution of B/S-TM in CIA mice

The *in vivo* distribution of B/S-TM after topical application of B/S-TM@MNs was investigated by IVIS (PerkinElmer, MA, USA). A hydrophobic infrared fluorescent dye DiR was utilized to label TM. CIA mice were subjected to anesthesia at 3, 6, 24, and 48 h post-application, and were subsequently visualized using an excitation wavelength of 740 nm and an emission wavelength of 780 nm. After imaging at the final time point, the mice were euthanized. Vital organs such as the heart, liver, spleen, lung, and kidneys, along with the entire hindlimbs of each mouse were collected for further *ex vivo* imaging.

2.13. Treatment of B/S-TM *in vivo*

The CIA mice were treated with saline, B-TM, S-TM, B/S-TM, B-TM@MN, S-TM@MN and B/S-TM@MN at a dose of 2 mg kg^{-1} ($n = 5$ per group). Treatment began on day 10 after the first injection of the model establishment, and was administered every three days for a total of eight treatments. Concurrently, healthy mice were maintained as a control group. The body weight and the clinical scores of four limbs of the mice were recorded every three days. The ankle diameter extending from the medial to the lateral aspect was accurately measured using a digital caliper at three-day intervals.

2.14. Micro-CT analysis

Upon treatment completion, all mice underwent micro-CT scans of their hind limbs using a microPET/CT system (Mediso, nanoScan PET/CT 82s, Budapest, Hungary). Three-dimensional reconstructions were created utilizing the RadiAnt DICOM Viewer (Medixant, Poland) for visualization.

2.15. *In vivo* cytokine evaluation

To assess the *in vivo* anti-inflammatory effects of B/S-TM@MN, serum levels of inflammatory factors were examined. Whole blood samples were collected from mice for centrifugation (1500 rpm, 20 min). Following plasma separation, serum levels of inflammatory factors, including TNF-α, IL-6, and IL-1β, were measured using a commercially available ELISA kit (Jiancheng, Nanjing, China) according to the manufacturer's instructions. Absorbance at 450 nm was documented using a microplate reader.

2.16. Histological analysis

Upon reaching the designated study endpoints, mice were euthanized to obtain the ankle joints for H&E, safranin-O and T&B staining. To analyze the *in vivo* anti-angiogenesis effect of B/S-TM, ankle joint sections were stained with anti-HIF-1α, anti-CD31, anti-VEGF, anti-ANG-1, anti-CD68 and anti-CD90 to perform immunohistochemistry (IHC) according to the standard protocol. The IHC images were captured by DMI8 inverted microscope.

2.17 Statistical analysis

The data were presented as the mean value ± standard deviation (SD). The statistical significance was determined using

the Student's *t*-test and one-way ANOVA, with analyses conducted using GraphPad Prism 7 (San Diego, CA, USA). Significance levels of *p < 0.05, **p < 0.01, and ***p < 0.001 were deemed indicative of a significant difference.

3. Results and discussion

3.1. Screening the optimal anti-inflammatory dose ratio of Ber and Sin

It is crucial to investigate the optimal therapeutic dose ratio of dual drugs before constructing the co-delivery nano-system. Hence, we first evaluated the cytotoxicity of Ber and Sin to macrophages and human umbilical vein endothelial cells (HUVECs), which are abundant cell populations in joints.

According to the MTT assay results, both Ber and Sin showed no obvious cytotoxicity to HUVECs under the concentration of 1 µg mL^{-1} (Fig. S1†). Then, we performed the *in vitro* macrophage phenotypic transition analysis to screen the optimal combined dose ratio of Ber and Sin according to the anti-inflammatory effects. These results revealed that the combination of Ber and Sin at the weight ratio of 1:1 exhibited the minimum M1 polarization (Fig. S2†), indicating the strongest efficacy of inhibiting inflammation.

3.2. Characterization of B/S-TM

The uniform-sized ROS-responsive micelles co-loaded with Ber and Sin (B/S-TM) were fabricated through the co-solvent evaporation method.[31] As shown in Fig. 1A, the average
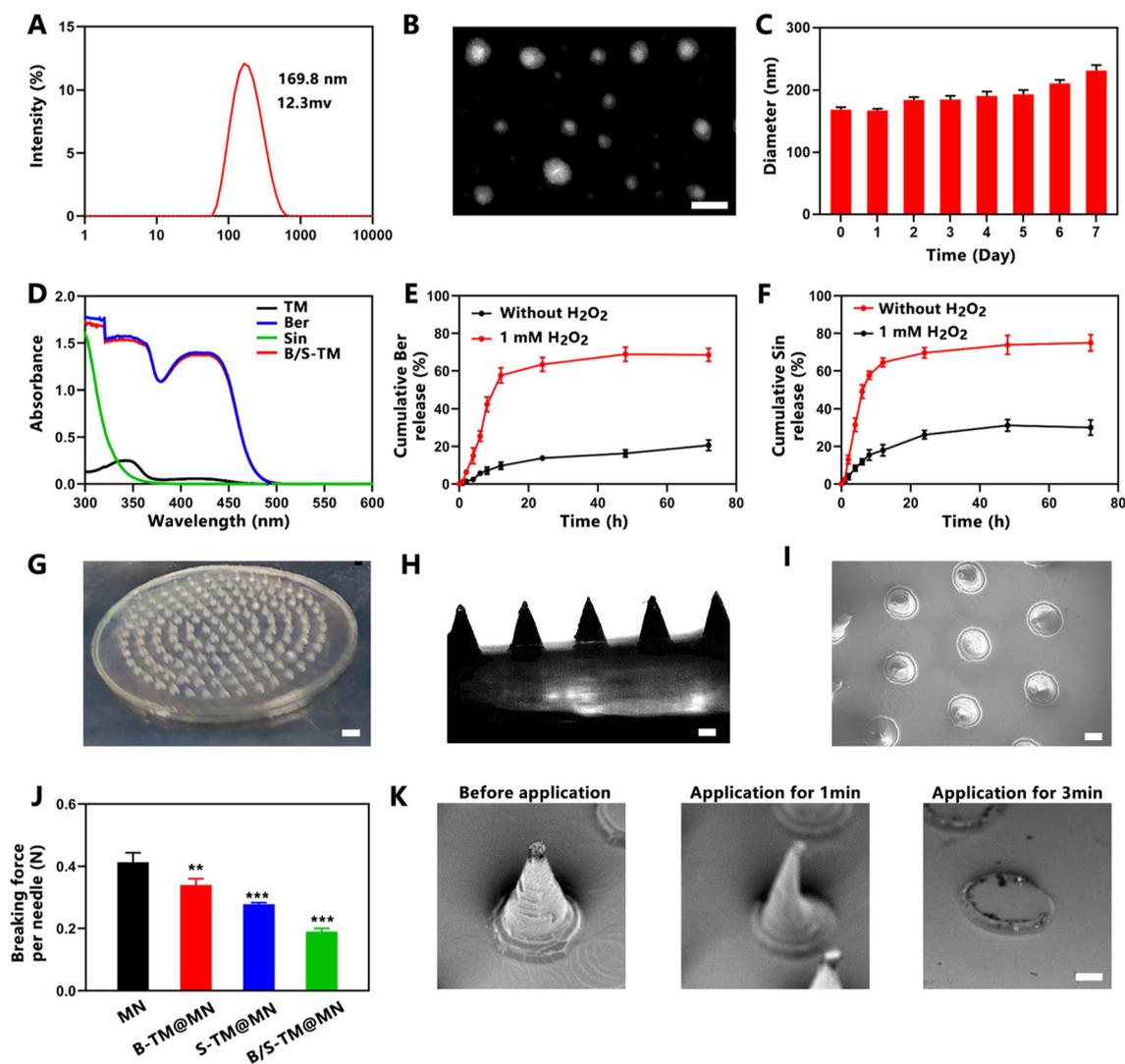

Fig. 1 Preparation and characterization of B/S-TM@MN. (A) Particle size distribution of B/S-TM analyzed using DLS. (B) Representative TEM image of B/S-TM. Scale bar: 200 nm. (C) Stability of B/S-TM during 7 days. (D) UV–vis spectra of blank micelle (TM), free Ber, free Sin and B/S-TM. *In vitro* Ber (E) and Sin (F) release from B/S-TM in the absence and presence of 1 mM H$_2$O$_2$. (G) Digital image of B/S-TM. Scale bar: 1 mm. (H) Microscopic morphology of B/S-TM. Scale bar: 200 µm. (I) SEM image of B/S-TM MN. Scale bar: 200 µm. (J) Mean breaking force per needle of blank MN, B-TM@MN, S-TM@MN and B/S-TM@MN. (K) SEM images of B/S-TM MN applied on pig skin for 30 min. Scale bar: 200 µm. Data are expressed as mean ± SD, n = 3. *p < 0.05, **p < 0.01, ***p < 0.001.

hydrodynamic diameter and the surface zeta potential of B/S-TM were 169.8 ± 2.1 nm and 12.3 ± 1.8 mV, as measured by dynamic light scattering (DLS). TEM images further displayed the uniform morphologies (Fig. 1B). Moreover, the particle size of B/S-TM remained stable and exhibited a slight increase during a period of 7 days (Fig. 1C). The UV-vis spectra of the blank micelle, free Ber, free Sin and B/S-TM are shown in Fig. 1D. Free Ber and B/S-TM exhibited similar absorbance spectra, which confirmed successful encapsulation of Ber. The encapsulation of Sin was further verified by HPLC method, and the encapsulation efficiencies of Ber and Sin were calculated as 85.7% ± 1.9% and 79.1% ± 3.2%, respectively. B/S-TM was anticipated to possess ROS-responsive ability due to the presence of the thioketal linker. As shown in Fig. 1E and F, the drug release profiles showed that the release rate of Ber and Sin from B/S-TM was only 20.6% ± 2.3% and 30.0% ± 3.2% within 72 h, while the release rate of Ber and Sin significantly increased in the presence of H_2O_2, reaching 68.5% ± 2.8% and 74.9% ± 3.5% after 72 h, respectively.

3.3. Characterization of B/S-TM@MN

B/S-TM@MN was prepared using a simple micro-molding method. B/S-TM@MN possessed a total of 136 needles with a conical structure, which were evenly distributed on a patch of approximately 4.3 cm². As shown in scanning electron microscopy (SEM) and optical microscopy images, the needles of B/S-TM@MN had a length of approximately 600 μm and a base diameter of 400 μm (Fig. 1G–I). Microneedles required sufficient mechanical strength to effectively pierce the skin and deliver B/S-TM into the inflamed joints. The average fracture force of B/S-TM@MNs were measured as 0.19 N per needle compared with the blank MN (0.41 N per needle). Although the addition of B/S-TM reduced the mechanical strength because it decreased the dense structure of sodium carboxymethylcellulose, the breaking force of B/S-TM@MNs still surpassed 0.058 N per needle, which is the minimum force reported to pierce human skin.[34] As shown in Fig. 2K, B/S-TM@MN dissolved rapidly within 1 min while the needles completely disappeared after 3 min, indicating the rapid dissolvable capacity.
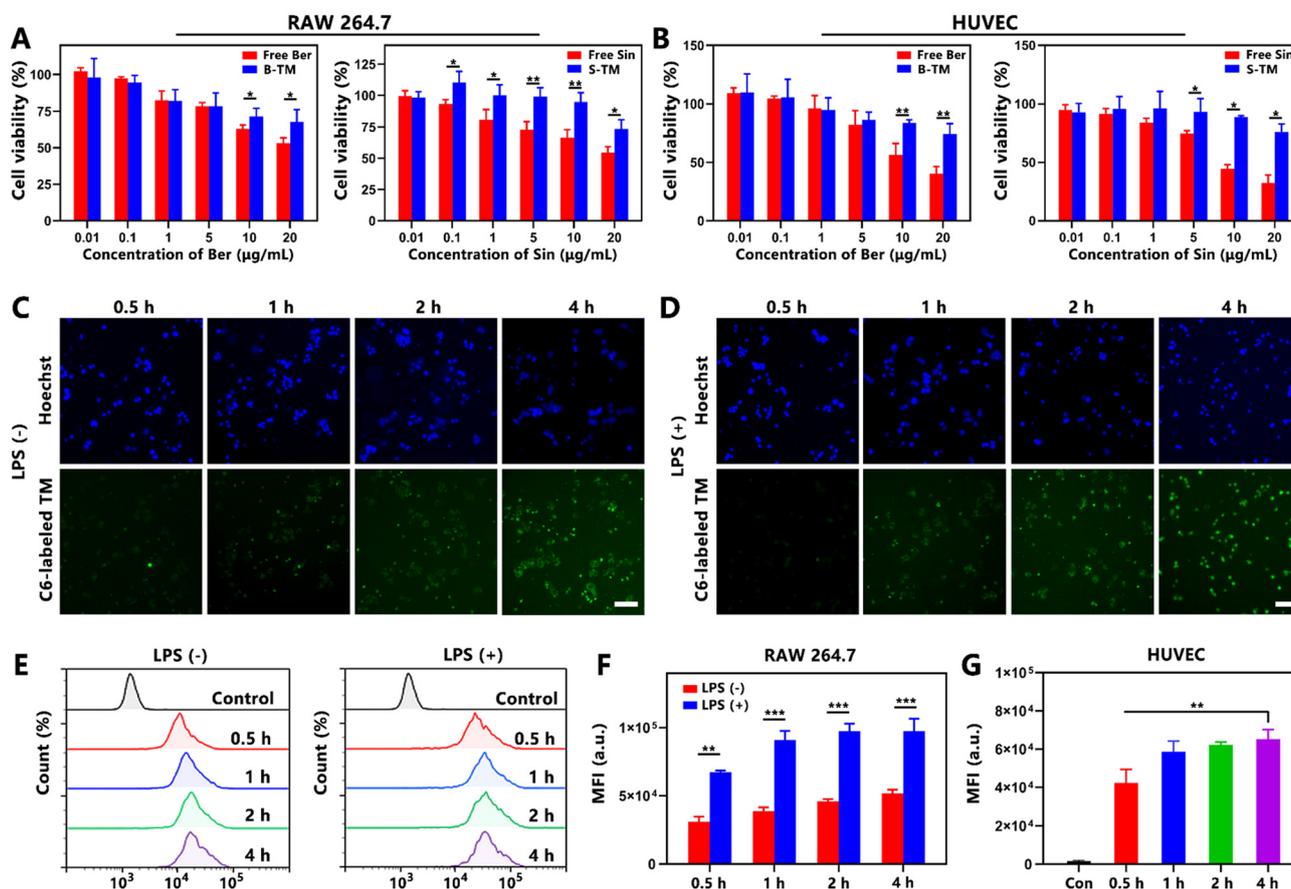
Fig. 2 Cytotoxicity and cellular uptake of B/S-TM in RAW 264.7 and HUVEC cells. Cell viability of RAW264.7 cells (A) and HUVEC cells (B) treated with free Ber, B-TM, free Sin and S-TM at different concentrations. Cellular uptake of C6-labeled TM in RAW264.7 cells without (C) or with (D) LPS stimulation (1 μg mL⁻¹) at 0.5 h, 1 h, 2 h and 4 h captured using a fluorescence microscope. Scale bar: 200 μm. (E) Flow cytometry analysis revealing the cellular uptake of C6-labeled TM in RAW 264.7 cells with or without LPS stimulation at different time points. Quantitative analysis of the cellular uptake in RAW 264.7 cells (F) and HUVEC cells (G) according to the flow cytometry result. Data are expressed as mean ± SD, n = 3. *p < 0.05, **p < 0.01, ***p < 0.001.

3.4. Cytotoxicity and cellular uptake of B/S-TM

The cytotoxicity of free Ber, free Sin, B-TM and S-TM was investigated against RAW 264.7 cells and HUVEC cells via MTT assay (Fig. 2A and B). The relative viability of RAW 264.7 and HUVEC cells treated with free Ber, free Sin, B-TM and S-TM both decreased when the concentration of Ber/Sin increased. B-TM and S-TM were less cytotoxic than free Ber/Sin especially in high concentrations ranging from 5–20 μg mL^{-1}, indicating that the encapsulation of TM could facilitate a reduction in the toxicity. Hydrophobic dye C6 was employed in place of Ber/ Sin to assess the cellular uptake of TM. The green fluorescence of RAW 264.7 cells with or without LPS stimulation was gradually enhanced, indicating efficient cellular uptake of C6-labeled TM in macrophages (Fig. 2C and D). The flow cytometry results further confirmed the high cellular uptake efficiency of C6-labeled TM in macrophages (Fig. 2E). Notably, the fluorescence intensity in activated macrophages by LPS was markedly higher than that in macrophages without LPS stimulation (Fig. 2F). Similarly, C6-labeled TM revealed the effective cellular uptake in HUVECs via the fluorescent images and FCS results (Fig. S3† and Fig. 2G). Therefore, TM lowered the cytotoxicity of payloads and exhibited excellent cellular uptake efficiency in both RAW 264.7 and HUVEC cells, which is advantageous to exerting the anti-inflammation and anti-angiogenesis activity of B/S-TM.

3.5. Inflammation inhibition capacity of B/S-TM

Since Ber and Sin are classical anti-inflammatory natural products employed in RA treatment,[35,36] the anti-inflammatory efficacy of B/S-TM was assessed by conducting the macrophage polarization analysis and cytokine evaluation (Fig. 3A). LPS was used to stimulate RAW 264.7 cells to attain the pro-inflammatory M1 phenotype macrophage. As exhibited in the flow cytometry result of Fig. 3B and C, the proportion of CD86-
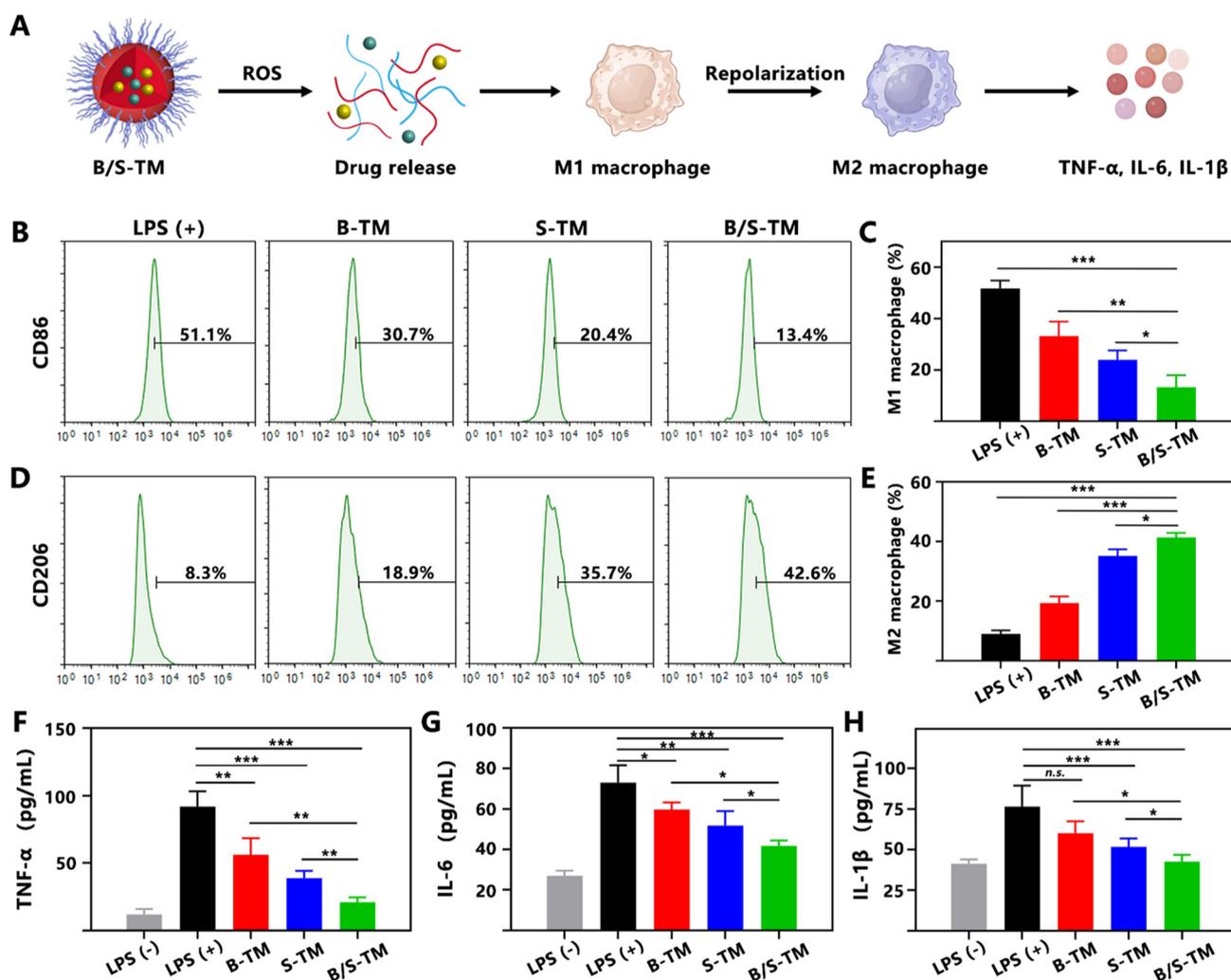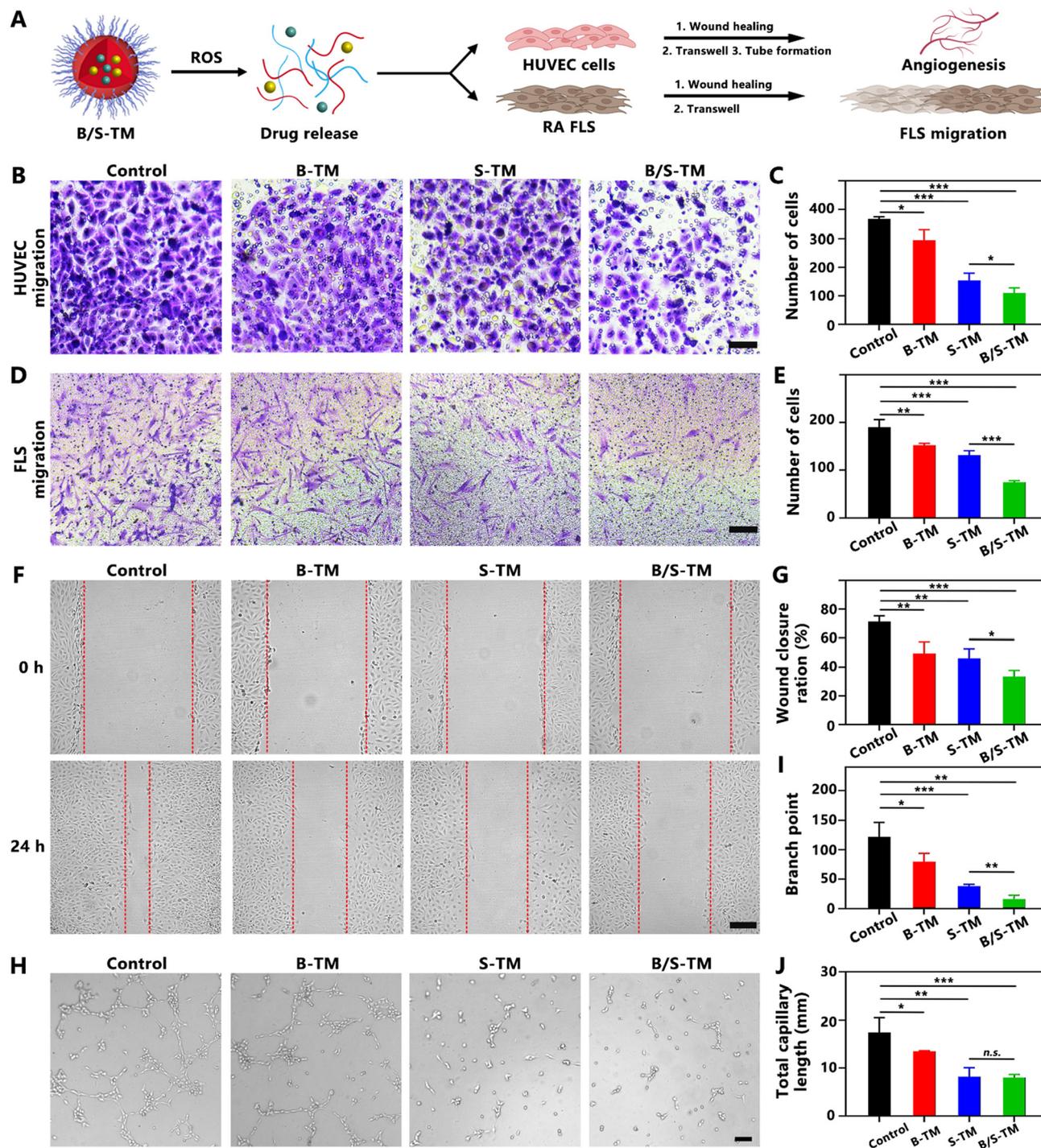

Fig. 3 *In vitro* anti-inflammation capacity of B/S-TM. (A) Illustration of B/S-TM for transforming M1 macrophages to M2 macrophages to decrease the pro-inflammatory cytokine secretion. CD86 (B) and CD206 expression levels (D) in LPS-stimulated RAW 264.7 cells treated with B-TM, S-TM and B/S-TM using flow cytometry analysis. Quantitative analysis of M1 (C) and M2 macrophage percentage (E). Levels of TNF-α (F), IL-6 (G) and IL-1β (H) in the supernatant fluid of RAW 264.7 cells after various treatments. Data are expressed as mean ± SD, $n = 3$. *$p < 0.05$, **$p < 0.01$, ***$p < 0.001$.

labeled M1 macrophage treated with B-TM and S-TM was significantly reduced to 33.2% ± 4.6% and 23.9% ± 2.9% compared with the LPS-treated group (51.7% ± 2.5%). B/S-TM

revealed a lower M1 polarization percentage of 13.3% ± 3.9%, suggesting an enhanced anti-inflammatory effect. Correspondingly, B-TM and S-TM increased the proportion of

Fig. 4 *In vitro* anti-angiogenesis and FLS migration inhibition capacity of B/S-TM. (A) Illustration of B/S-TM exerting an anti-angiogenesis and FLS migration inhibition effect for RA treatment. Transwell assay results of HUVECs (B) and FLS (D) treated with PBS, B-TM, S-TM and B/S-TM for 24 h. Scale bar: 50 μm. Quantitative analysis of Transwell assay results of HUVECs (C) and FLS (E). (F) Representative wound healing images of HUVECs after treatment with PBS, B-TM, S-TM and B/S-TM for 24 h. Scale bar, 200 μm. (G) Quantitative analysis of migration areas in the wound healing assay. (H) Representative tube formation images of VEGF-induced HUVECs after incubation with PBS, B-TM, S-TM and B/S-TM for 12 h. Scale bar: 100 μm. Quantitative analysis of the branch point (I) and total capillary length (J). Data are expressed as mean ± SD, $n = 3$. $*p < 0.05$, $**p < 0.01$, $***p < 0.001$.

CD206-labeled M2 macrophage from 8.9% ± 1.0% to 19.3% ± 1.8% and 35.2% ± 1.8%, respectively (Fig. 3D and E). The percentage of M2 macrophages was further increased to 41.4% ± 1.2% after treatment by the B/S-TM group. The levels of TNF-α, IL-6 and IL-1β in the culture supernatant were also investigated for further verifying the inflammation inhibition effect of B/S-TM. As shown in Fig. 3F–H, S-TM showed a stronger inhibitory effect than B-TM in lowering the secretion of pro-inflammatory cytokines. Furthermore, B/S-TM further decreased the level of these cytokines compared with B-TM or S-TM, which was consistent with the macrophage polarization result. These results revealed that B/S-TM could effectively facilitate the transition from M1 to M2 polarization and attenuate the levels of pro-inflammatory cytokines.

3.6. Anti-angiogenesis effect of B/S-TM

The synovial hyperplasia and pannus formation as crucial pathological features of RA relate to angiogenesis and fibroblast-like synoviocyte (FLS) migration (Fig. 4A). Angiogenesis is a multifaceted process encompassing the migration of endothelial cells, microvessel sprouting, tubule formation, and stabilization of newly formed vessels. It plays a crucial role in the pathogenesis of inflammatory autoimmune diseases, including systemic sclerosis, psoriasis and rheumatoid arthritis.[37,38] Anti-angiogenesis in the RA joint contributes to reducing synovitis and pannus formation.[39,40] Therefore, the anti-angiogenesis property of B/S-TM was also evaluated by performing HUVEC migration, wound healing and tube forming assay. The migration of HUVECs was significantly suppressed after incubation of B-TM, S-TM and B/S-TM to a certain extent (Fig. 4B). B/S-TM revealed a stronger inhibitory efficacy than B-TM, S-TM in reducing the number of migrated HUVECs due to the combined effect (Fig. 4C). In the wound healing assay, the wound closure ratio reached 71.4% ± 3.2% in the PBS control group after 24 h. By contrast, the wound closure ratios were significantly reduced to 49.6% ± 6.4%, 46.2% ± 5.3% and 33.6% ± 3.5% after treatment with B-TM, S-TM and B/S-TM, respectively (Fig. 4F and G), which was consistent with the Transwell migration result. As shown in Fig. 4H, B-TM partially inhibited the tube formation trend, while S-TM and B/S-TM exhibited a higher inhibition effect on tube formation. Compared with the control group, the branch point was reduced by 34.7%, 68.6% and 86.6% for the B-TM, S-TM and B/S-TM group, respectively (Fig. 4I). A similar trend could be also observed in the quantitative result of the total capillary length (Fig. 4J). Notably, Ber and Sin have also been reported to inhibit FLS migration, which is critical for halting RA progression, as hypermigratory FLS directly mediates synovial hyperplasia, cartilage invasion, and osteoclast activation.[41,42] Hence, we further investigated the therapeutic effect of B/S-TM on inhibiting FLS migration. Both B-TM and S-TM showed no cytotoxicity to FLS at a high concentration of 20 μg mL^{-1} (Fig. S4†). The therapeutic effect of B/S-TM in inhibiting FLS migration was confirmed by Transwell and wound healing assay, which was better than B-TM or S-TM

(Fig. 4D–E and Fig. S5, S6†). These data demonstrated the effective anti-angiogenesis and FLS migration inhibition capacity of B/S-TM, exhibiting its potential in preventing synovial hyperplasia and pannus formation.

3.7. In vivo distribution of B/S-TM@MN in CIA mice

To evaluate the *in vivo* distribution of B/S-TM released from B/S-TM@MN, a CIA mouse model with inflammation joints was developed. DiR-labeled TM@MN was topically applied at the back of the RA mice. Interestingly, B/S-TM exhibited rapid accumulation in the RA-affected joints, reaching a maximum at 3 h (Fig. 5A and B). The effective accumulation of B/S-TM over the duration of 48 h could be attained by microneedle-mediated transdermal delivery, which is promising for patients requiring chronic therapy to reduce pain and invasiveness compared with traditional intravenous injection and intraarticular injection. Additionally, *ex vivo* imaging of the major organs and hind limbs after 48 h corroborated the highest distribution of B/S-TM in the RA-afflicted joints (Fig. 5C and D). These results substantiate the efficient accumulation and retention of B/S-TM at the inflammation sites.
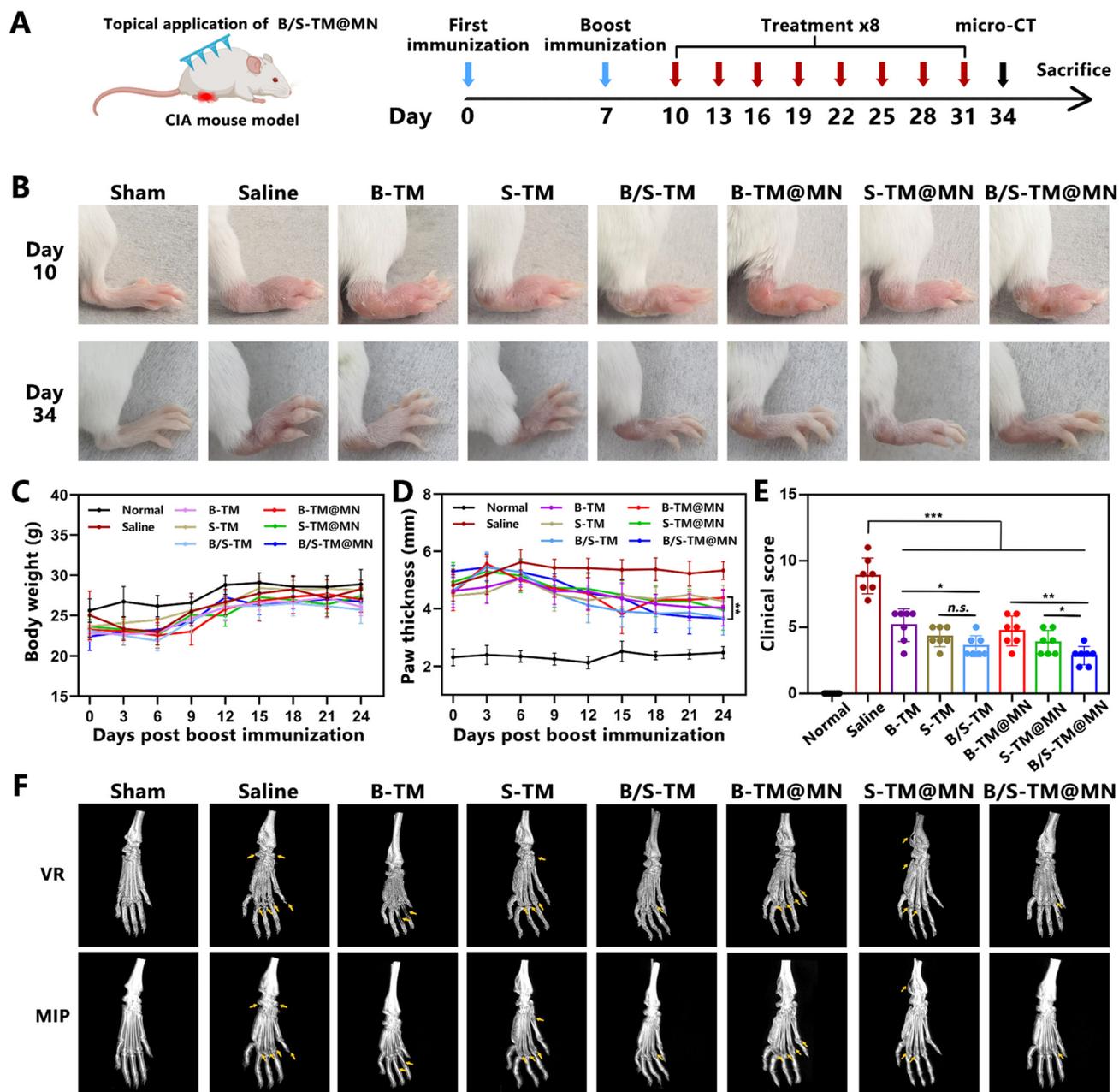
3.8. In vivo anti-arthritis efficacy of B/S-TM@MN in CIA mice

Inspired by the integrated anti-inflammation and anti-angiogenesis capacity of B/S-TM@MN, the combinatorial therapeutic effects were evaluated in RA model mice with CIA. The
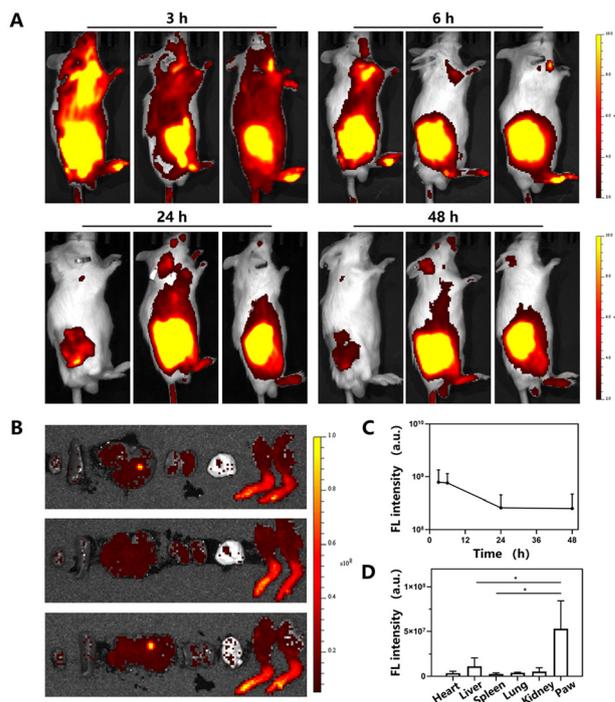
Fig. 5 Distribution of B/S-TM@MN in CIA mice. (A) Fluorescence images of DiR-labeled B/S-TM@MN in CIA mice at 3, 6, 24, and 48 h after topical application. (B) *Ex vivo* imaging of the major organs and hind legs of CIA mice treated with DiR-labeled B/S-TM@MN after 48 h. (C) Fluorescence intensity of paws at different times. (D) Fluorescence intensity of the major organs after 48 h.

Fig. 6 *In vivo* anti-arthritis efficacy of the B/S-TM@MN in CIA mouse model. (A) Schematic of RA treatment. CIA mice receiving various treatments 8 times every three days from day 10 to day 31, followed by sacrifice on day 34. Ber, 2 mg kg^{-1}; Sin 2 mg kg^{-1}, ($n = 6$). (B) Representative images of paws in CIA mice treated with B-TM, S-TM, B/S-TM, B-TM@MN, S-TM@MN and B/S-TM@MN. (C) Body weight changes in 24 days post-boost immunization. Paw thickness (D) and clinical scores (E) of paws in CIA mice after various treatments. (F) Micro-CT images of the paws of CIA mice in different treatment groups processed *via* volume rendering (VR) and maximal intensity projection (MIP) techniques. The yellow arrows indicate skeletal damage and destruction. Data are expressed as mean ± SD, $n = 6$. *$p < 0.05$, **$p < 0.01$, ***$p < 0.001$.

timelines of arthritis establishment and functional microneedle treatment are exhibited in Fig. 6A. Representative inflamed hind paw images of collagen-induced arthritic mice after different treatments are presented in Fig. 6B. The mice in the B-TM@MN, S-TM@MN and B/S-TM@MN groups showed less paw swelling and ankylosis compared with the saline group. In addition, the B/S-TM@MN group displayed more alleviated symptoms of arthritis than the B-TM@MN and S-TM@MN

groups, which revealed a similar trend in the groups of subcutaneously injecting B-TM, S-TM, and B/S-TM. The body weight of mice in different treatments had little change during the experiments (Fig. 6C). Furthermore, the paw swelling degree was assessed by measuring the paw thickness, while clinical scores were used to reflect the disease progression control (Fig. 6D and E). The paw thickness and clinical scores exhibited a marked increase in the saline group, while these indexes

were partially lowered in the B-TM@MN and S-TM@MN groups. Better therapeutic effects were observed in the B/S-TM@MN group than those of the B-TM@MN and S-TM@MN group, which could be attributed to the simultaneous anti-inflammatory and anti-angiogenesis effects. Micro-CT analysis was performed to characterize the bone erosion and damage. As shown in Fig. 6F, the saline group exhibited a rough bone surface and pronounced ankle bone

loss extending from the calcaneus bones to the phalanges. The bones of the mice in the B/S-TM@MN group exhibited a smoother surface, and maintained a more stable structure in the ankle joints compared to those in the B-TM@MN and S-TM@MN groups. These results demonstrated that the combinatorial treatment *via* anti-inflammation and anti-angiogenesis resulted in a notable remission of the physiological symptoms.
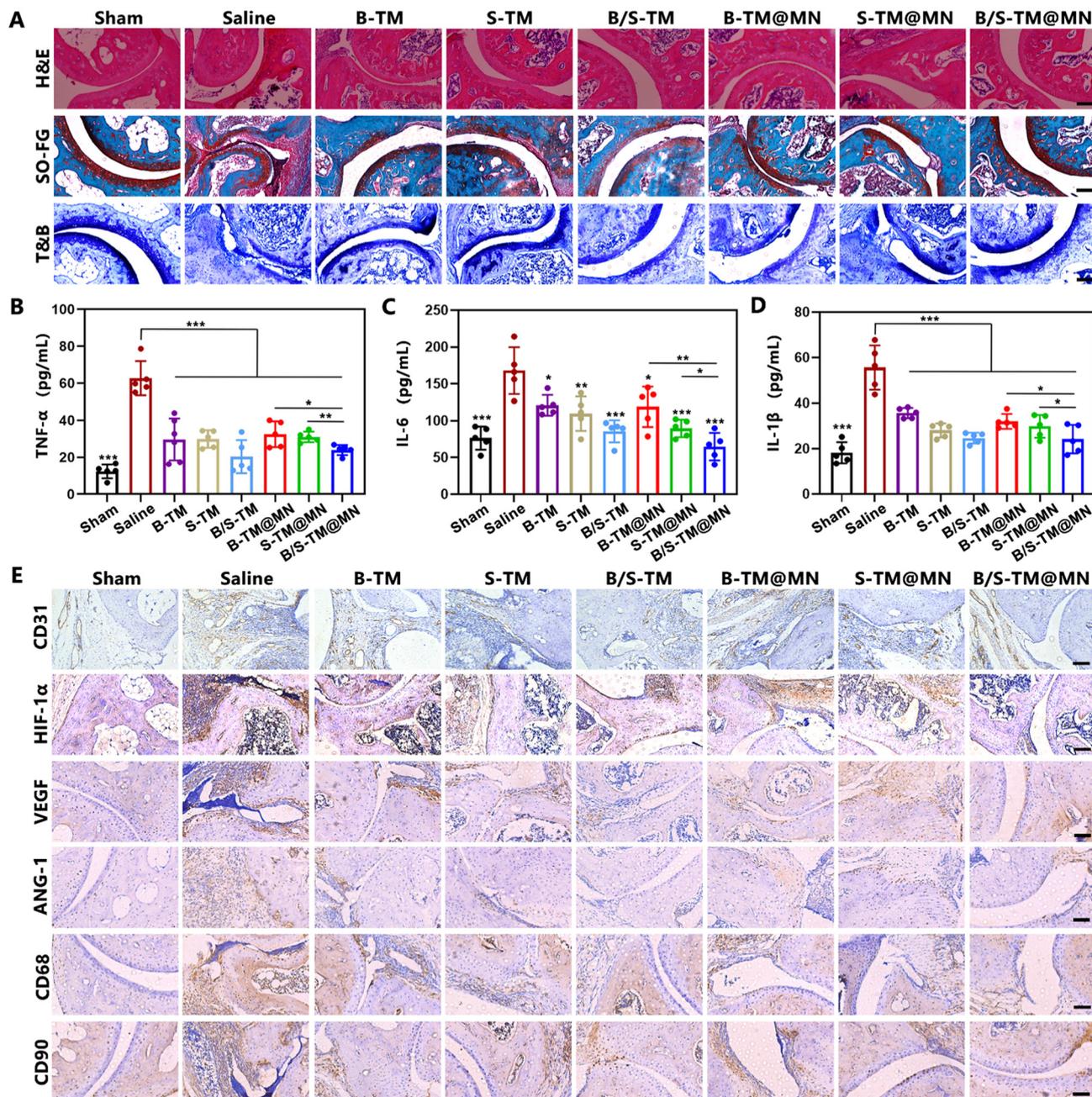

Fig. 7   *In vivo* pathologic condition assessments and mechanisms of therapeutic efficacy after treatment with B/S-TM@MN. (A) Histological assays with H&E staining, safranin O/fast green staining and T&B staining. Scale bar: 100 μm. Levels of TNF-α (B), IL-6 (C) and IL-1β (D) in serum measured using ELISA assay. (E) Representative IHC images of CD31, HIF-1α, VEGF, ANG-1, CD68, CD90. Scale bar: 100 μm. Data are expressed as mean ± SD, $n = 6$. *$p < 0.05$, **$p < 0.01$, ***$p < 0.001$.

3.9. Histological and *in vivo* pro-inflammatory cytokine evaluation

We next performed histological analysis of the ankle joint sections upon completion of the treatments to further assess the anti-arthritis efficacy of B/S-TM@MN. Extensive pannus formation and significant bone destruction in the saline group was observed in the Hematoxylin and eosin (H&E) staining images. In contrast, the B/S-TM@MN group showed no discernible bone erosion or pannus formation (Fig. 7A). The joint conditions in the B-TM@MN and S-TM@MN groups were superior to that in the saline group, yet worse than the B/S-TM@MN group. Safranin O images used for glycosaminoglycans staining also exhibited similar trends in cartilage preservation. Prominent proteoglycan loss was evident in the saline group, indicating severe articular cartilage damage. Conversely, the cartilage structures were well-preserved in the B/S-TM@MN group, demonstrating noticeably superior therapeutic efficacy compared to the B-TM@MN and S-TM@MN groups. T&B staining further verified the chondroprotective effect of B/S-TM@MN. Then, the *in vivo* levels of TNF-α, IL-6 and IL-1β were determined by ELISA kits (Fig. 7B–D). Consistent with the *in vitro* result, both B-TM@MN and S-TM@MN could lower the pro-inflammatory cytokine levels to a certain extent for inflammation alleviation. The levels of TNF-α, IL-6 and IL-1β were further decreased after treatment by B/S-TM@MN. The immunohistochemistry assay was implemented to evaluate the expression of CD31 within the synovial tissue of articulations due to CD31 expression reflecting the microvessel density. A notable abundance of CD31 staining was observed within the synovium in the saline group, whereas CD31 staining was considerably reduced in the B-TM@MN, S-TM@MN and B/S-TM@MN groups (Fig. 7E, and Fig. S7†). The B/S-TM@MN group revealed the lowest microvessel density in the ankle joints of CIA mice. We further monitored the levels of hypoxia-inducible factor-1α (HIF-1α), vascular endothelial growth factor (VEGF) and angiopoietin-1 (ANG-1) by immunohistochemistry assay, which play essential roles in angiogenesis regulation. The high expression of HIF-1α, VEGF and ANG-1 in CIA mice was also partially downregulated after treatment by B-TM@MN and S-TM@MN. B/S-TM@MN exhibited the best inhibitory effect in the expression of HIF-1α, VEGF and ANG-1, which was consistent with the result of the microvessel density. Moreover, the cell specific markers including CD68 (macrophages) and CD90 (FLS) were also evaluated to reflect the abundance change of the macrophages and RA FLS after treatment. B/S-TM@MN significantly reduced the population of macrophages and RA FLS, which also demonstrated the excellent anti-arthritis effect of B/S-TM@MN. In addition, no obvious tissue damage was observed in the H&E images of major organs (Fig. S8†), indicating the basic safety profile of B/S-TM@MN. Overall, these results confirmed the effective anti-inflammation and anti-angiogenesis activity of B/S-TM@MN, which achieved excellent anti-arthritis efficacy in alleviating constant synovitis, cartilage damage and bone erosion.

4. Conclusions

As synovial inflammation and angiogenesis play essential roles in RA progression, we developed a nanomedicine-integrated dissolvable microneedle patch (B/S-TM@MN) that can inhibit inflammation to enhance the overall anti-arthritis outcome. The ROS-responsive B/S-TM was rapidly released from microneedle, absorbed by blood vessels in the corium layer, and accumulated in inflamed joints due to the ELVIS effect. The controlled release of Ber and Sin was achieved through the cleavage of thioketal groups triggered by the high level of ROS in the RA joint microenvironment. The combination of Ber and Sin demonstrated effective alleviation of inflammation and inhibition of angiogenesis, leading to significant relief of synovial inflammation and reversal of bone and cartilage damage in the CIA mouse model. As a feasible and multifunctional platform, B/S-TM@MN offers a potential therapeutic strategy for treatments of RA and other inflammatory diseases characterized by pathological angiogenesis.

Author contributions

Peng Hua: conceptualization, formal analysis, investigation, validation, visualization, writing – original draft, review & editing. Suleixin Yang: formal analysis. Lin Yu: writing – review & editing. Yongzhuo Huang: supervision. Meiwan Chen: conceptualization, funding acquisition, supervision, writing – review & editing.

Data availability

Data will be made available on request.

Conflicts of interest

The authors declare no conflicts of interest.

Acknowledgements

References

1 J. S. Smolen, D. Aletaha and I. B. McInnes, *Lancet*, 2016, **388**, 2023–2038.

2 A. Finckh, B. Gilbert, B. Hodkinson, S. C. Bae, R. Thomas, K. D. Deane, D. Alpizar-Rodriguez and K. Lauper, *Nat. Rev. Rheumatol.*, 2022, **18**, 591–602.

3 S. W. Tas, C. X. Maracle, E. Balogh and Z. Szekanecz, *Nat. Rev. Rheumatol.*, 2016, **12**, 111–122.

4 A. Alaarg, C. Pérez-Medina, J. M. Metselaar, M. Nahrendorf, Z. A. Fayad, G. Storm and W. J. M. Mulder, *Adv. Drug Delivery Rev.*, 2017, **119**, 143–158.

5 S. Konisti, S. Kiriakidis and E. M. Paleolog, *Nat. Rev. Rheumatol.*, 2012, **8**, 153–162.

6 A. G. Arroyo and M. L. Iruela-Arispe, *Cardiovasc. Res.*, 2010, **86**, 226–235.

7 A. Meyer, S. R. Zack, W. Nijim, A. Burgos, V. Patel, B. Zanotti, M. V. Volin, M. A. Amin, M. J. Lewis, C. Pitzalis, S. Arami, J. A. Karam, N. J. Sweiss and S. Shahrara, *Cell. Mol. Immunol.*, 2024, **21**, 33–46.

8 C. Costa, J. Incio and R. Soares, *Angiogenesis*, 2007, **10**, 149–166.

9 M. A. Amin, P. L. Campbell, J. H. Ruth, T. Isozaki, B. J. Rabquer, W. Alex Stinson, M. O'Brien, G. Edhayan, R. A. Ohara, J. Vargo, S. E. Domino and A. E. Koch, *Ann. Rheum. Dis.*, 2015, **74**, 1459–1466.

10 X.-x. Fan, M.-z. Xu, E. L.-H. Leung, C. Jun, Z. Yuan and L. Liu, *Nano-Micro Lett.*, 2020, **12**, 76.

11 Z.-M. Jiang, S.-L. Zeng, T.-Q. Huang, Y. Lin, F.-F. Wang, X.-J. Gao, J. Li, P. Li and E. H. Liu, *Sci. Bull.*, 2023, **68**, 1540–1555.

12 Y. Lin, O. Yi, M. Hu, S. Hu, Z. Su, J. Liao, W. Wang, S. Wang, L. Liu, B. Liu and X. Cai, *J. Controlled Release*, 2022, **348**, 42–56.

13 K. Y. Lu, Y. C. Lin, H. T. Lu, Y. C. Ho, S. C. Weng, M. L. Tsai and F. L. Mi, *Carbohydr. Polym.*, 2019, **206**, 664–673.

14 J. M. Li, Y. D. Yao, J. F. Luo, J. X. Liu, L. L. Lu, Z. Q. Liu, Y. Dong, Y. Xie and H. Zhou, *Phytomedicine*, 2023, **121**, 155114.

15 D. N. Huang, F. F. Wu, A. H. Zhang, H. Sun and X. J. Wang, *Pharmacol. Res.*, 2021, **169**, 105667.

16 X. Ai, P. Yu, L. Luo, J. Sun, H. Tao, X. Wang and X. Meng, *J. Ethnopharmacol.*, 2022, **296**, 115453.

17 Z. T. Feng, T. Yang, X. Q. Hou, H. Y. Wu, J. T. Feng, B. J. Ou, S. J. Cai, J. Li and Z. G. Mei, *Biomed. Pharmacother.*, 2019, **113**, 108759.

18 C. Liu, W. Su, X. Jiang, F. Kong, Q. Chen, Q. Zhang, H. Zhang, Y. Liu, X. Li, X. Xu, Y. Chen and D. Qu, *Adv. Healthcare Mater.*, 2024, 2303659.

19 Y. Jin, Y. Guo, J. Yang, X. Chu, X. Huang, Q. Wang, Y. Zeng, L. Su, S. Lu, C. Wang, J. Yang, J. Qu, Y. Yang and B. Wang, *Adv. Mater.*, 2023, **35**, 2209690.

20 B. Tang, W. Ma and Y. Lin, *J. Controlled Release*, 2023, **364**, 61–78.

21 X. Luan, X. Zhang, M. Nie and Y. Zhao, *Research*, 2023, **6**, 0141.

22 L. Fan, X. Zhang, M. Nie, Y. Xu, Y. Wang, L. Shang, Y. Zhao and Y. Zhao, *Adv. Funct. Mater.*, 2022, **32**, 2110746.

23 P. Hua, R. Liang, S. Yang, Y. Tu and M. Chen, *Bioact. Mater.*, 2024, **36**, 83–95.

24 Y. Zhao, X. Chen, P. He, X. Wang, Y. Xu, R. Hu, Y. Ou, Z. Zhang, Z. Zhang, G. Du and X. Sun, *Small*, 2023, e2307366, DOI: **10.1002/smll.202307366**.

25 F. Qu, R. Geng, Y. Liu and J. Zhu, *Theranostics*, 2022, **12**, 3372–3406.

26 S. Liang, Z. Li, C. Bao, B. Liu, H. Zhang, Y. Yuan, H. Yan, S. Chen, H. Zhang, W. Shi, F. Ren and Y. Li, *Small*, 2023, **19**, 2301751.

27 K. Peng, L. K. Vora, I. A. Tekko, A. D. Permana, J. Domínguez-Robles, D. Ramadon, P. Chambers, H. O. McCarthy, E. Larrañeta and R. F. Donnelly, *J. Controlled Release*, 2021, **339**, 361–380.

28 P. Hua, R. Liang, Y. Tu, Y. Yin, M.-K. Law and M. Chen, *Acta Pharm. Sin. B*, 2023, **13**, 5016–5029.

29 F. Zhou, M. Li, M. Chen, M. Chen, X. Chen, Z. Luo, Z. Cai and Y. Hu, *ACS Nano*, 2023, **17**, 4358–4372.

30 X. X. Fan, M. Z. Xu, E. L. Leung, C. Jun, Z. Yuan and L. Liu, *Nano-Micro Lett.*, 2020, **12**, 76.

31 R. Liang, K. H. Wong, Y. Yang, Y. Duan and M. Chen, *Biomater. Sci.*, 2022, **10**, 1018–1025.

32 B. Wang, W. Zhang, Q. Pan, J. Tao, S. Li, T. Jiang and X. Zhao, *Nano Lett.*, 2023, **23**, 1327–1336.

33 D. D. Brand, K. A. Latham and E. F. Rosloniec, *Nat. Protoc.*, 2007, **2**, 1269–1275.

34 X. Ning, C. Wiraja, D. C. S. Lio and C. Xu, *Adv. Healthcare Mater.*, 2020, **9**, 2000147.

35 X. Peng, Y. Yang, C. Guo, Q. He, Y. Li, T. Gong and J. Li, *Front. Pharmacol.*, 2023, **14**, 1210129.

36 Y. Lin, O. Yi, M. Hu, S. Hu, Z. Su, J. Liao, W. Wang, S. Wang, L. Liu, B. Liu and X. Cai, *J. Controlled Release*, 2022, **348**, 42–56.

37 H. A. Elshabrawy, Z. Chen, M. V. Volin, S. Ravella, S. Virupannavar and S. Shahrara, *Angiogenesis*, 2015, **18**, 433–448.

38 E. Romano, M. Manetti, I. Rosa, B. S. Fioretto, L. Ibba-Manneschi, M. Matucci-Cerinic and S. Guiducci, *Ann. Rheum. Dis.*, 2018, **77**, 1665–1674.

39 Y. Wang, Z. Liu, T. Li, L. Chen, J. Lyu, C. Li, Y. Lin, N. Hao, M. Zhou and Z. Zhong, *Theranostics*, 2019, **9**, 708–720.

40 A. A. Mohammad, L. C. Phillip, H. R. Jeffrey, I. Takeo, J. R. Bradley, W. A. Stinson, O. Martin, E. Gautam, A. O. Ray, V. Jonathon, E. D. Steven and E. K. Alisa, *Ann. Rheum. Dis.*, 2015, **74**, 1459.

41 F. Xu, C. Shen, S. Zhang, Y. Liu, D. Liu, Y. Kuang, R. Li, C. Wang, X. Cai, M. Shi and Y. Xiao, *Int. Immunopharmacol.*, 2024, **128**, 111433.

42 Y. Ou, W. Li, X. Li, Z. Lin and M. Li, *Rheumatol. Int.*, 2011, **31**, 1479–1485.